Exploring the making of a galactic wind in the starbursting dwarf irregular galaxy IC 10 with LOFAR

Downloaded from: https://research.chalmers.se, 2025-12-05 04:40 UTC

Citation for the original published paper (version of record):
Heesen, V., Rafferty, D., Horneffer, A. et al (2018). Exploring the making of a galactic wind in the starbursting dwarf irregular galaxy IC 10 with
LOFAR. Monthly Notices of the Royal Astronomical Society, 476(2): 1756-1764.
http://dx.doi.org/10.1093/mnras/sty325

N.B. When citing this work, cite the original published paper.

research.chalmers.se offers the possibility of retrieving research publications produced at Chalmers University of Technology. It covers all kind of research output: articles, dissertations, conference papers, reports etc. since 2004. research.chalmers.se is administrated and maintained by Chalmers Library

(article starts on next page)

Monthly Notices
of the
ROYAL ASTRONOMICAL SOCIETY

MNRAS **476,** 1756–1764 (2018) doi:10.1093/mnras/sty325
Advance Access publication 2018 February 9

Exploring the making of a galactic wind in the starbursting dwarf irregular galaxy IC 10 with LOFAR

V. Heesen,[1]★ D. A. Rafferty,[1] A. Horneffer,[2] R. Beck,[2] A. Basu,[2,3] J. Westcott,[4] L. Hindson,[4] E. Brinks,[4] K. T. Chyży,[5] A. M. M. Scaife,[6] M. Brüggen,[1] G. Heald,[7,8] A. Fletcher,[9] C. Horellou,[10] F. S. Tabatabaei,[11,12] R. Paladino,[13] B. Nikiel-Wroczyński,[4,5] M. Hoeft[14] and R.-J. Dettmar[15]

[1]*Hamburger Sternwarte, Universität Hamburg, Gojenbergsweg 112, D-21029 Hamburg, Germany*
[2]*Max-Planck-Institut für Radioastronomie, Auf dem Hügel 69, D-53121 Bonn, Germany*
[3]*Fakultät für Physik, Universität Bielefeld, Postfach 100131, D-33501 Bielefeld, Germany*
[4]*School of Physics, Astronomy and Mathematics, University of Hertfordshire, Hatfield AL10 9AB, UK*
[5]*Astronomical Observatory, Jagiellonian University, ul. Orla 171, PL-30-244 Kraków, Poland*
[6]*Jodrell Bank Centre for Astrophysics, Alan Turing Building, Oxford Road, Manchester M13 9PL, UK*
[7]*CSIRO Astronomy and Space Science, 26 Dick Perry Avenue, Kensington, WA 6151, Australia*
[8]*Kapteyn Astronomical Institute, University of Groningen, NL-9700 AV Groningen, the Netherlands*
[9]*School of Mathematics and Statistics, Newcastle University, Newcastle-upon-Tyne NE1 7RU, UK*
[10]*Department of Space, Earth and Environment, Chalmers University of Technology, Onsala Space Observatory, SE-439 92 Onsala, Sweden*
[11]*Instituto de Astrofísica de Canarias, Vía Láctea S/N, E-38205 La Laguna, Spain*
[12]*Departamento de Astrofísica, Universidad de La Laguna, E-38206 La Laguna, Spain*
[13]*INAF/Istituto di Radioastronomia, via Gobetti 101, I-40129 Bologna, Italy*
[14]*Thüringer Landessternwarte (TLS), Sternwarte 5, D-07778 Tautenburg, Germany*
[15]*Astronomisches Institut der Ruhr-Universität Bochum, D-44780 Bochum, Germany*

Accepted 2018 February 1. Received 2018 January 26; in original form 2017 November 7

ABSTRACT

Low-mass galaxies are subject to strong galactic outflows, in which cosmic rays may play an important role; they can be best traced with low-frequency radio continuum observations, which are less affected by spectral ageing. We present a study of the nearby starburst dwarf irregular galaxy IC 10 using observations at 140 MHz with the Low-Frequency Array (LOFAR), at 1580 MHz with the Very Large Array (VLA), and at 6200 MHz with the VLA and the 100-m Effelsberg telescope. We find that IC 10 has a low-frequency radio halo, which manifests itself as a second component (thick disc) in the minor axis profiles of the non-thermal radio continuum emission at 140 and 1580 MHz. These profiles are then fitted with 1D cosmic ray transport models for pure diffusion and advection. We find that a diffusion model fits best, with a diffusion coefficient of $D = (0.4\text{–}0.8) \times 10^{26} (E/\mathrm{GeV})^{0.5}\,\mathrm{cm^2\,s^{-1}}$, which is at least an order of magnitude smaller than estimates both from anisotropic diffusion and the diffusion length. In contrast, advection models, which cannot be ruled out due to the mild inclination, while providing poorer fits, result in advection speeds close to the escape velocity of $\approx$50 km s^{-1}, as expected for a cosmic ray-driven wind. Our favoured model with an accelerating wind provides a self-consistent solution, where the magnetic field is in energy equipartition with both the warm neutral and warm ionized medium with an important contribution from cosmic rays. Consequently, cosmic rays can play a vital role for the launching of galactic winds in the disc–halo interface.

Key words: cosmic rays – galaxies: magnetic fields – radio continuum: galaxies.

★ E-mail: volker.heesen@hs.uni-hamburg.de

© 2018 The Author(s)
Published by Oxford University Press on behalf of the Royal Astronomical Society

1 INTRODUCTION

Galactic winds are an important ingredient in galaxy evolution, removing angular momentum and energy over a galaxy's lifetime (e.g. Veilleux, Cecil & Bland-Hawthorn 2005). Such winds are thought to be prevailing in dwarf irregular galaxies, which have burst-like star formation histories and weak gravitational potentials (Tremonti et al. 2004). Because dwarf galaxies are the building blocks of galaxy formation in the early Universe and are the most abundant type of galaxies, it has been suggested that galactic winds in them can explain the metal enrichment of the intergalactic medium at high redshifts (Recchi & Hensler 2013). Cosmic rays have long been suspected to play a part in the launching of galactic winds, their cooling being much slower than that of the hot, supernovae-heated gas (Breitschwerdt, McKenzie & Völk 1991). This idea has recently been addressed again in several theoretical papers (e.g. Pakmor et al. 2016) with the conclusion that cosmic rays could play an important role in launching galactic winds. On the observational side this can be explored by studying the synchrotron emission of cosmic ray electrons (CREs) spiralling around the magnetic field lines – this emission is the non-thermal component of the radio continuum emission from galaxies.

Aside from this aspect of studying the importance of cosmic rays for the physics of the interstellar medium (ISM), radio continuum emission in galaxies is an important tracer for the star formation rate (SFR), unobscured by dust and observable with ground-based telescopes (Heesen et al. 2014; Tabatabaei et al. 2017). Radio interferometers have the necessary angular resolution in order to study nearby galaxies at 100-pc scales that allows us to explore the physical processes behind the radio–SFR relation. At GHz and even MHz frequencies, where the non-thermal emission dominates over the thermal (free–free) emission, a galaxy may be either (i) an *electron calorimeter*, i.e. the CREs are confined within the galaxy and radiate all their energy away (Völk 1989); or (ii) there may be *energy equipartition* between the cosmic rays and the magnetic field and a relation between the magnetic field strength (B) and the SFR (Niklas & Beck 1997). Of course, intermediate states may also exist. Present-day observations of spiral galaxies seem to favour model (ii) and galactic winds can be a mechanism to remove CREs and attain energy equipartition. Furthermore, a B–SFR relation can be realized in an elegant way, by assuming a constant velocity dispersion in the ISM, which is a good approximation, and a Kennicutt–Schmidt relation between the SFR and the gas density (ρ). A B–ρ, and thus a B–SFR, relation is then a consequence if the magnetic energy density is in equipartition with the kinetic energy density of the ISM (Heesen et al. 2014).

In this paper, we present a low-frequency radio continuum study of the nearby starburst dwarf irregular galaxy IC 10 to shed new light on the interplay between magnetic fields, cosmic rays, and star formation. In particular, we would like to explore whether a radio halo exist and, if so, whether it can be explained with a cosmic ray-driven wind such as found in late-type spiral edge-on galaxies (Heesen et al. 2018b). Owing to its proximity ($D = 0.7$ Mpc), this galaxy is particularly well suited for such an investigation since we can study the ISM at sub-kpc scales (1 arcsec $\approx$ 3.39 pc). Low frequencies are advantageous for such work. First, dwarf irregular galaxies have a high thermal contribution to their radio continuum emission (typically 30 per cent at 1.4 GHz rather than 10 per cent as in spiral galaxies; Tabatabaei et al. 2017). Hence, going to $\approx$140 MHz is expected to reduce the thermal fraction to a 10- or 20-per cent level; this is because the thermal radio continuum emission depends only weakly on frequency ($\propto \nu^{-0.1}$), whereas the non-thermal part increases at low frequencies ($\propto \nu^{-0.6}$, typically). Second, low frequencies allow us to explore the synchrotron emission of CREs far away from star formations sites that cannot be detected at GHz frequencies due to spectral ageing. Such a study has now become possible with the advent of the Low-Frequency Array (LOFAR; van Haarlem et al. 2013), which combines high angular resolution ($\approx$10 arcsec) with a sensitivity that is approximately matched with other state-of-the-art interferometers operating at GHz frequencies such as the Karl G. Jansky Very Large Array (VLA).

IC 10 is considered a dwarf irregular galaxy (dynamical mass of $1.6 \times 10^8\,\mathrm{M}_\odot$; Oh et al. 2015) currently undergoing a starburst, owing to its high number of Wolf–Rayet stars (Massey & Armandroff 1995). It has a large supply of atomic hydrogen, detected as H I line emission in the radio, suggesting that the galaxy has accreted a large supply of hydrogen in recent times, which is able to sustain its current high star formation surface density $\Sigma_{\mathrm{SFR}} \approx 10^{-1}\,\mathrm{M}_\odot\,\mathrm{yr}^{-1}\,\mathrm{kpc}^{-2}$ (Hunter et al. 2012). IC 10 has been studied extensively in the radio continuum as well. Chyży et al. (2016) showed that the galaxy has ordered magnetic fields, which are arranged in a similar pattern (X-shaped) as has been found in nearby edge-on spiral galaxies. They suggest that the galaxy has a spherical outflow as found in magnetohydrodynamic (MHD) simulations of dwarf galaxies. IC 10 has several massive H II regions, of which the south-eastern star formation complex hosts a 150-pc non-thermal superbubble, likely the result of a few supernovae or one massive hypernova in the last few Myr (Heesen et al. 2015). A recent low-frequency study of Basu et al. (2017) concentrated on the spatially resolved radio–SFR relation; they showed that the relation holds down to 50-pc spatial resolution in the disc close to the star formation sites. Westcott et al. (2017) used high-resolution radio continuum observations to investigate the nature of the compact sources in IC 10; they were shown to be either background active galactic nuclei (AGNs) or internal H II regions.

This paper is organized as follows. In Section 2, we outline our observations and data reduction of our new LOFAR observations. Section 3 presents our results together with those from archival VLA and Effelsberg data. In Section 4, we model the radio continuum data with 1D cosmic ray transport in order to measure diffusion coefficients and advection speeds. These models, which are either for pure diffusion along magnetic field lines or for pure advection in a galactic wind, allow us to separate the cosmic ray and magnetic energy densities without the assumption of (local) energy equipartition. In Section 5, we then study the relation between cosmic rays, magnetic fields, and the other constituents to the ISM such as the warm neutral and warm ionized medium. We summarize and present our conclusions in Section 6.

2 OBSERVATIONS

Observations with the LOFAR high-band antenna (HBA) system were taken on 2013 August 25 and 26 in the HBA_DUAL_INNER configuration as part of the observing programme LC0_43. The observations were taken in interleaved mode, with alternating scans of the calibrator 3C 48 (2 min) and the target (12 min). The data were reduced with the novel 'facet calibration' technique, which mitigates the direction-dependent effects of the ionosphere and beam response that impact low-frequency radio continuum observations with aperture arrays, so that images close to the thermal noise level can be obtained (van Weeren et al. 2016; Williams et al. 2016). First, the (u, v) data are calibrated with direction-independent methods

using the PREFACTOR pipeline.[1] This pipeline first calibrates 3C 48 using the Scaife & Heald (2012) flux densities, assuming a point-like source. From the resulting gain solutions the instrumental components are extracted: the station gain amplitudes and the phase variations due to the drift of the clocks of the LOFAR stations. The latter is separated from the variations due to the changing total electron content (TEC) of the ionosphere with the clock–TEC separation. These instrumental calibration solutions are applied to the target data, which are then averaged to 10-s time resolution and two channels per subband frequency resolution (channel width of 97.656 kHz). The data are calibrated in phase only using the Global Sky Model (GSM; Scheers 2011), which is a compilation of sources from the VLA Low-frequency Sky Survey Redux (VLSSr; Lane et al. 2014), the Westerbork Northern Sky Survey (WENSS; Rengelink et al. 1997), and the NRAO VLA Sky Survey (NVSS; Condon et al. 1998). With the direction-independent calibration applied, the (u, v) data are inverted and deconvolved with a wide-field CLEAN algorithm. As final step of PREFACTOR, the CLEAN components of all the sources within the ≈8° field of view (FOV) are subtracted from the (u, v) data.

The residual, direction-independent calibrated (u, v) data with all sources subtracted, together with the subtracted model and the solutions of the phase-only calibration, are then the input for the direction-dependent facet calibration, for which we used the FACTOR pipeline (Rafferty et al., in preparation).[2] The FOV was divided into 55 facets around calibrator regions with integrated 177-MHz flux densities (of the full facet) between 0.3 and 12 Jy. Of those, the seven brightest facets were processed one at a time, with the faintest facet having a flux density of 2.1 Jy. The facet calibration technique allows us to track and correct for the direction-dependent effects of the Earth's ionosphere (effectively the 'seeing' at long radio wavelengths) and the station beam response by first self-calibrating on the calibrator region of a facet and then using the solutions to update the model for the full facet, which in turn is used to update the residual (u, v) data. In the first step of the calibration, fast, 10-s phase solutions are determined in small chunks of ≈2 MHz bandwidth to correct for the positional change and distortion of sources. In the second step, slow, tens-of-minutes amplitude solutions are used to track the variation of the apparent flux density of a source. The target facet was corrected using the solution of a nearby, 0.°9 away, facet at RA 00$^{\rm h}$15$^{\rm m}$50.$^{\rm s}$76, Dec. 58°36′23.″47 (J2000.0) with a 177-MHz flux density of 5.4 Jy.

For the final data set we used observations of 23 core stations, each acting as two stations, and 13 remote stations, 5.4 h of on-source time with 49.2 MHz bandwidth. The direction-dependent calibrated (u, v) data were taken into the Common Astronomy Software Applications (CASA; McMullin et al. 2007) and inverted and deconvolved with the MS–MFS CLEAN algorithm (Rau & Cornwell 2011). We fitted for the frequency dependence of the sky model (nterms = 2) and used angular scales of up to 600 arcsec diameter. The (u, v) range was restricted to 0.14–22.0 kλ, in order to match the L-band VLA observations in B- and C-arrays (see below); we used an outer taper of ≈40 arcsec with Briggs weighting, setting robust = 0. This resulted in a 140-MHz image with 44.0 × 42.3 arcsec^2 resolution (PA = 17.°4) with an rms noise level of 700 μJy beam^{-1}; this image of the target facet is presented in Fig. 1(a).[3] This is the map we use in what follows unless mentioned otherwise. We also created a high-resolution map using all (u, v) data and no taper with a resolution of 12.0 × 12.0 arcsec^2 and a rms noise level of 300 μJy beam^{-1}.

In addition, we created a 1580-MHz map from VLA observations in B- and C-arrays, already presented in Heesen et al. (2015). We used the same techniques as for the LOFAR 140-MHz image; the resulting map has a resolution of 43.3 × 41.4 arcsec^2 (PA = 27.°8) with an rms noise level of 70 μJy beam^{-1}. We also used a 6200-MHz map from VLA D-array observations, combined with observations from the 100-m Effelsberg telescope (Basu et al. 2017). This map has a resolution of 9.4 × 7.3 arcsec^2 (PA = −54.°6) and an rms noise level of 15 μJy beam^{-1}.

3 RESULTS

In Fig. 1(b), we show an overlay of our 140-MHz map as contours on a map of the integrated H I emission line intensity from the Local Irregulars That Trace Luminosity Extremes, The H I Nearby Galaxy Survey (LITTLE THINGS; Hunter et al. 2012) as colour-scale. The same contours are overlaid in Fig. 1(c) on the map of the thermal radio continuum emission, also at 140 MHz, which was constructed from Hα emission line maps (Gil de Paz, Madore & Pevunova 2003; Hunter & Elmegreen 2004) and corrected for foreground and internal absorption (see below). Fig. 1(d) shows this map with a logarithmic scaling, where we overlaid 140-MHz contours at 12 arcsec resolution. As can be seen, the low-frequency radio continuum emission does not correspond morphologically to either the warm neutral or the warm ionized medium. The radio continuum emission extends significantly into the halo with an extent of the 3σ contour line of 10.7 arcmin (2.2 kpc) along the minor axis and 7.3 arcmin (1.5 kpc) along the major axis (PA = −38°; Hunter et al. 2012), as shown by the blue lines in Figs 1(b) and (c). Assuming an inclination angle of $i = 47°$ (Oh et al. 2015), we would expect a minor axis extension of only ≈5 arcmin (≈1.0 kpc).

We do not find any indication for the spherical 'synchrotron envelope', which Chyży et al. (2016) detected using 1430-MHz VLA observations. This can be explained by the flat radio spectral index in the halo of IC 10. The integrated 140-MHz flux density of IC 10 is 756 ± 29 mJy, where we excluded sources 1 and 2 (Fig. 1d), which are unrelated background sources; source 1 has the morphology of a head–tail radio galaxy and source 2 that of a Fanaroff–Riley type II (FRII) radio galaxy (Fanaroff & Riley 1974). The integrated 1580-MHz flux density is 306 ± 10 mJy, resulting in a 140–1580 MHz spectral index of −0.38 ± 0.02.[4] Thus, the increased noise level in our LOFAR observations, compared with the VLA observations of Chyży et al. (2016), is not compensated by a steep spectrum and our data are less sensitive by comparison.

We subtract the contribution from the thermal radio continuum emission with a combination of Hα, *Spitzer* 24-μm mid-infrared and 32-GHz radio continuum emission (Heesen et al. 2015; Basu et al. 2017). The foreground absorption was corrected with $A_V = 2.59 \times E(B-V)$ using $E(B-V) = 0.75$ mag (Burstein &

[1] https://github.com/lofar-astron/prefactor
[2] https://github.com/lofar-astron/factor

[3] Angular resolutions in this paper are referred to as the full width at half-maximum (FWHM).
[4] Source 3 (see Fig. 2), likely a background AGN (Westcott et al. 2017), is included in this measurement since it is marginally detected only at 12 arcsec resolution (3.5σ) but cannot be separated from the background emission at 44 arcsec resolution.

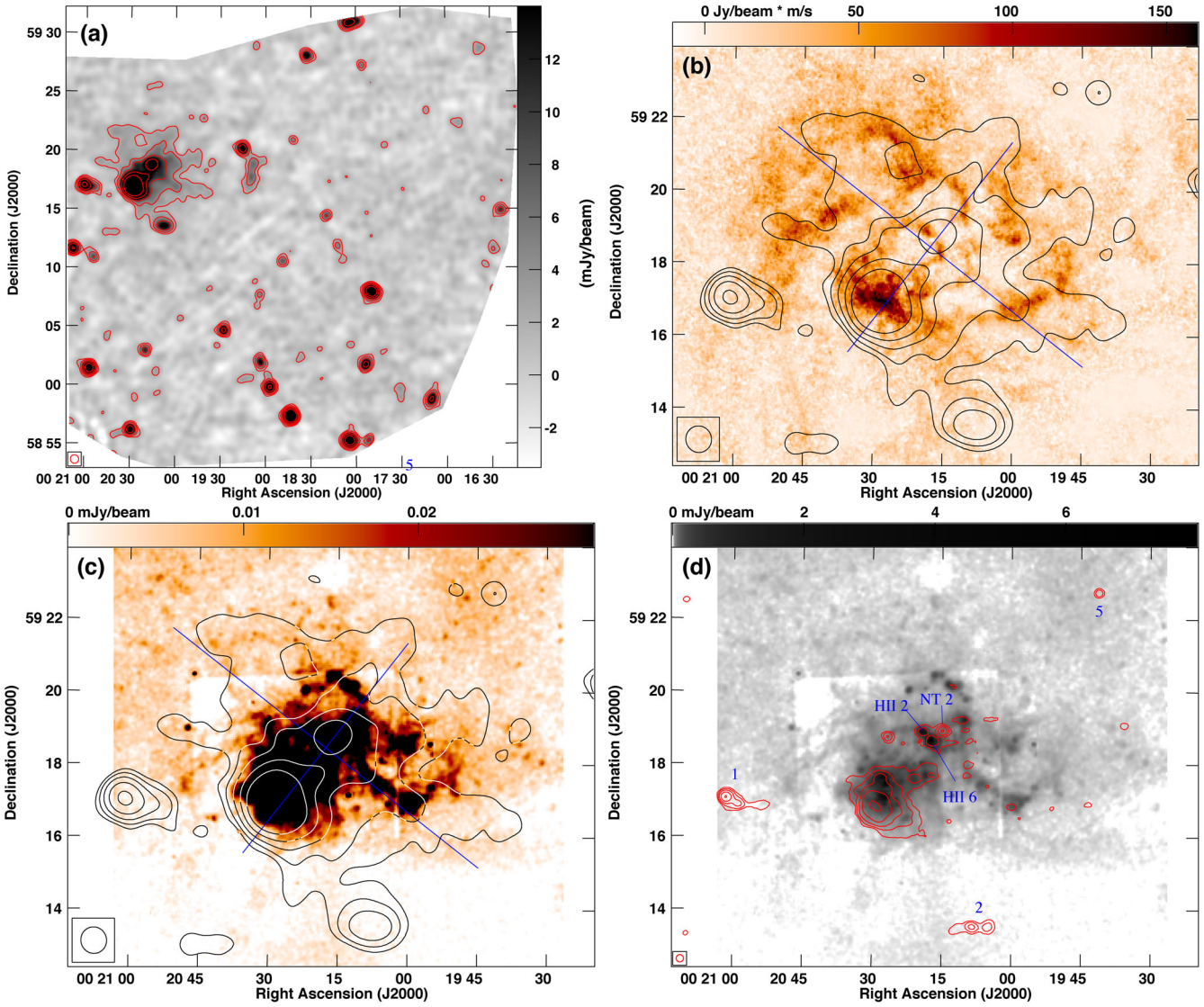

Figure 1. (a) Full target facet, where the LOFAR 140-MHz radio continuum emission at 44.0 × 42.3 arcsec^2 resolution is shown as contours, overlaid on the same emission as grey-scale. Contours are at $2^n \times 3\sigma$, with $n = 1, 2, 3, 4$ and $\sigma = 700$ μJy beam^{-1}. (b) Zoom in on IC 10, showing an area of approximately 2.9 × 2.3 kpc^2, where 140-MHz contours are overlaid on an integrated H I emission map from LITTLE THINGS survey at 5.9 × 5.5 arcsec^2 resolution. Contour levels as in panel (a). (c) Same area as in panel (b), where 140-MHz contours are overlaid on the thermal 140-MHz radio continuum emission at 6 × 6 arcsec^2 resolution. The thermal radio continuum was estimated from a combination of Hα, *Spitzer* 24-μm and VLA 32-GHz emission. Contour levels as in panel (a). (d) Same area as in panel (b), where LOFAR 140-MHz contours at a resolution of 12 × 12 arcsec^2 are overlaid on the 140-MHz thermal radio continuum emission as in panel (c). Contour levels are at $2^n \times 4\sigma$, with $n = 0, 1, 2, 3, 4$ and $\sigma = 300$ μJy beam^{-1}. In panels (b) and (c), blue lines show the major and minor axes of the radio continuum emission. Note that the shorter line is coincident with the optical major axis (PA = −38°). In all panels, the size of the synthesized beam of the LOFAR map is shown in the bottom left-hand corner.

Heiles 1984). The correction for internal absorption was done with the *Spitzer* 24-μm mid-infrared data (Kennicutt et al. 2009) using the flux densities of Bendo, Galliano & Madden (2012). This extinction corrected Hα map was then combined with a 32-GHz VLA map of the south-eastern H II region (see Heesen et al. 2015, for details). This results in an integrated thermal flux density of 161 ± 5 mJy at 140 MHz. Hence, the non-thermal integrated radio spectral index between 140 and 1580 MHz is −0.50 ± 0.03, which is consistent with the radio spectral index of ≈−0.5, expected for freshly injected CREs. The radio spectral index is also marginally consistent with the power-law fit between 320 and 24 500 MHz (0.55 ± 0.04; Basu et al. 2017) and the injection radio spectral index in the non-thermal superbubble (0.55 ± 0.05; Heesen et al. 2015).

There are several reasons why the non-thermal radio continuum spectrum may deviate from a power law, showing a flattening towards low frequencies. First, below ≈1 GHz, some of the compact radio continuum sources show a spectral turn-over (increasing flux density with frequency) due to thermal (free–free) absorption (Basu et al. 2017). This is in particular the case for source 4 (Fig. 2), which is unresolved at 44.0 × 42.3 arcsec^2 resolution but can be resolved into three components at 12.0 × 12.0 arcsec^2 resolution, two of which are H II regions (sources H II 2 and 6; Fig. 1d) and one is an unrelated non-thermal background AGN (source NT 2; Westcott et al. 2017). Source H II 2 shows a marginal spectral downturn at 320 MHz (Basu et al. 2017), which does not manifest itself at 140 MHz. The downturn of source H II 6, however, can be

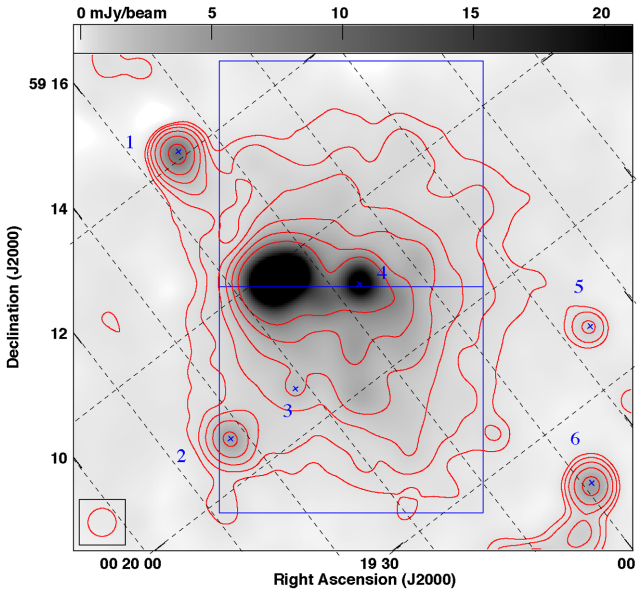

Figure 2. Non-thermal radio continuum emission at 1580 MHz with an angular resolution of 44.0 × 44.0 arcsec^2. Contours are $2^n \times 3\sigma$, with $n = 0, 1, 2, \ldots, 5$ and $\sigma = 70$ μJy beam^{-1}. The map has been rotated, so that the major axis of the radio continuum emission is horizontal. The minor axis strip used for the averaging along with the masked sources is shown as well. The size of the synthesized beam is shown in the bottom left-hand corner, which corresponds to a spatial resolution of ≈150 pc.

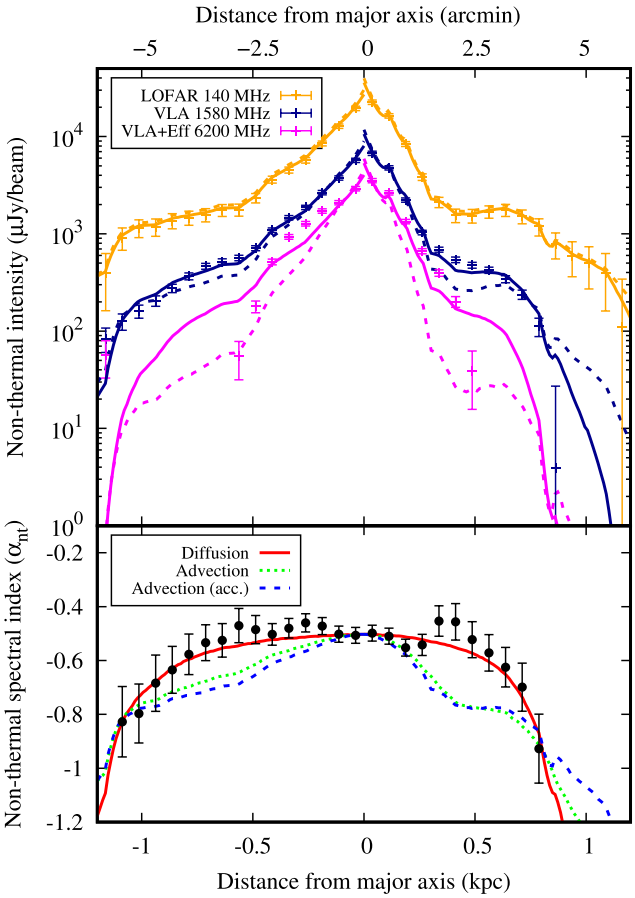

Figure 3. Minor axis profiles with distances from the major axis as seen on the sky. In the top panel, data points show the non-thermal radio continuum intensities at 140, 1580, and 6200 MHz. Solid lines show the best-fitting diffusion model (Model I, $\mu = 0.5$) and dashed lines our favoured model, which is advection with an accelerating wind (Model III). Note that the 140-MHz intensities are almost identical for both models. In the bottom panel, data points show the non-thermal radio spectral index between 140 and 1580 MHz. The various lines show the best-fitting models, where the solid red line shows the diffusion model (Model I, $\mu = 0.5$), the short-dashed green line the advection model with constant wind speed (Model II) and the long-dashed blue line the advection model with an accelerating wind (Model III). All models assume $\gamma_{\rm inj} = 2.0$ and the north-eastern halo is on the right-hand side ($z > 0$ kpc) and the south-western halo on the left-hand side ($z < 0$ kpc). Error bars show $\pm 1\sigma$ uncertainties as calculated in Section 3.

confirmed; it has a 140-MHz flux density of only ≈4 mJy, whereas the expected flux density is ≈14 mJy if the source would be following a power law. Still, the difference in spectral index is only $\Delta\alpha = +0.01$, which is not enough to explain the spectral flattening. In the diffuse ISM, thermal absorption is not expected to play a role. A second reason could be the escape of low-energy CREs in a galactic wind, which should be visible as a radio halo.

In order to investigate the existence of extraplanar emission and hence that of a radio halo further, we created minor axis profiles of the non-thermal radio continuum emission. We convolve the non-thermal radio continuum maps at 140, 1580, and 6200 MHz to 44.0 × 44.0 arcsec^2 resolution and rotate them, so that the radio major axis lies horizontal. As an example, we show in Fig. 2 the 1580-MHz map. Again, as with the 140-MHz map, the emission extends prominently along the minor axis. The contours are box shaped rather than of elliptical shape, so that emission away from the major axis could be extraplanar emission that is located above the star formation sites in the disc. This is the sign for the existence of a radio halo, where the emission extends vertically away from the star-forming disc but not radially (Dahlem, Lisenfeld & Rossa 2006). We have averaged the radio continuum emission within a strip along the minor axis, centred on RA 00$^{\rm h}$20$^{\rm m}$17$^{\rm s}$.732, Dec. 59°18′27″.24, with a width of 6.9 arcmin (1.4 kpc) and a height of 11.8 arcmin (2.4 kpc), spacing data points by 22 arcsec (≈75 pc, equivalent to FWHM/2), and masking unrelated background sources and those with spectral turn-overs (sources 1–4). In addition, we masked source 5, which is unresolved, and source 6, which has the morphology of an FRII radio galaxy; both have non-thermal spectral indices (≈−0.6) and are likely unrelated to IC 10. Error estimates of the intensities were calculated as $\delta I_\nu^2 = (\epsilon_I I_\nu)^2 + \sigma_{\rm b}^2$, where $\epsilon_I = 0.05$ is the calibration uncertainty and $\sigma_{\rm b} = \sigma/\sqrt{N}$ is the intensity base level uncertainty with N the number of beams within the integration region. The non-thermal radio spectral index error is then

$$\delta\alpha_{\rm nt} = \frac{1}{\left|\ln\left(\frac{\nu_1}{\nu_2}\right)\right|}\sqrt{\left(\frac{\delta I_1}{I_1}\right)^2 + \left(\frac{\delta I_2}{I_2}\right)^2}, \quad (1)$$

where I_1 and I_2 are the non-thermal radio continuum intensities at frequencies ν_1 and ν_2, respectively.

The resulting minor axis profiles of the non-thermal radio continuum emission at 140, 1580, and 6200 MHz and of the non-thermal radio spectral index between 140 and 1580 MHz are presented in Fig. 3. As can be seen, the 140- and 1580-MHz profiles show a good correspondence everywhere. We detect a break in the intensity profiles at a major axis distance of ≈0.5 kpc, where the decrease of the intensity with increasing distance significantly flattens. We interpret this as the transition from the projected galactic disc to

the halo emission, where the thick disc corresponds to the halo emission. The distance of 0.5 kpc from the major axis corresponds to the projected length of the semimajor axis, $\cos(i) \times 1.5\,\mathrm{kpc}/2$, which is the distance from the major axis up to which emission from the galactic disc still contributes. The 6200-MHz profile can be only traced out to 0.5 kpc distance from the major axis, at larger distances the emission decreases rapidly. Hence, we do not detect a radio halo at 6200 MHz. At all frequencies, the profiles show the expected behaviour for spectral ageing.

The existence of a radio halo can be further corroborated by a 3D toy model, which is then converted into synthetic intensity maps. We created a 'disc' model that has a vertical intrinsic intensity scale height of 0.1 kpc and a 'halo' model with a vertical intrinsic intensity scale height of 0.5 kpc. The synchrotron emissivity is constant for galactocentric radii $\leq$0.7 kpc and vanishes outside of this cylinder with a diameter of 1.4 kpc. These cylindrical models were tilted away from edge-on, corresponding to the inclination angle of $i = 47^\circ$, and the emissivity was integrated along the line of sight. The resulting synthetic intensity distribution and minor axis intensity profile are shown in Fig. 4. Clearly, the disc model cannot explain the observed intensity profile at distances >0.5 kpc from the major axis, whereas the halo model can. Thus, the existence of a halo is required to account for the observations.

4 COSMIC RAY TRANSPORT

We now use the low-frequency radio spectral index information in order to study the transport of CREs away from the star formation sites, which are located near the galactic mid-plane. We have used the software SPINNAKER (Spectral Index Numerical Analysis of K(c)osmic-ray Electron Radio-emission), which calculates vertical synchrotron emission profiles for stationary 1D cosmic ray transport models for either pure advection or diffusion (Heesen et al. 2016).[5] We assume that the CREs are injected near the major axis and are transported vertically away in the direction of the minor axis. We did not deproject vertical distances for the inclination, so that the distance to the major axis as seen on the sky, z, is assumed to be the travelling distance of the cosmic rays. Since the galactic disc of IC 10 is tilted significantly away from edge-on, we potentially underestimate the travelling distances of the CREs by a factor of $1/\sin(i) = 1.37$. However, simply deprojecting distances would overcorrect for the shortening because the projected width of the outflow $\cos(i) \times 1.4\,\mathrm{kpc} = 0.5\,\mathrm{kpc}$ contributes to the observed height with an almost identical ratio: (halo height+projected outflow width)/(halo height) =1.7 kpc/1.2 kpc = 1.4. This is corroborated by our synthetic intensity maps. The intensity scale height of the halo model in Fig. 4 as measured on the sky is 0.45 kpc; hence, the intrinsic scale height, taking into account line-of-sight integration of an inclined cylinder, corresponds to an effective correction for deprojection of 1.1 that is close to 1.0, so we simply use the distance as measured on the sky.

The profiles at 140 and 1580 MHz are fitted for an injection index, γ_{inj}, where the CREs are injected in the mid-plane with a number density of $N(E, z = 0) \propto E^{-\gamma_{\mathrm{inj}}}$. The CRE number density is evolved as function of distance from a solution of the diffusion–loss equation, where the losses are due to synchrotron and inverse Compton radiation and adiabatic losses (Heesen et al. 2018a). Following this, the non-thermal radio continuum intensity is computed

[5] https://github.com/vheesen/spinnaker

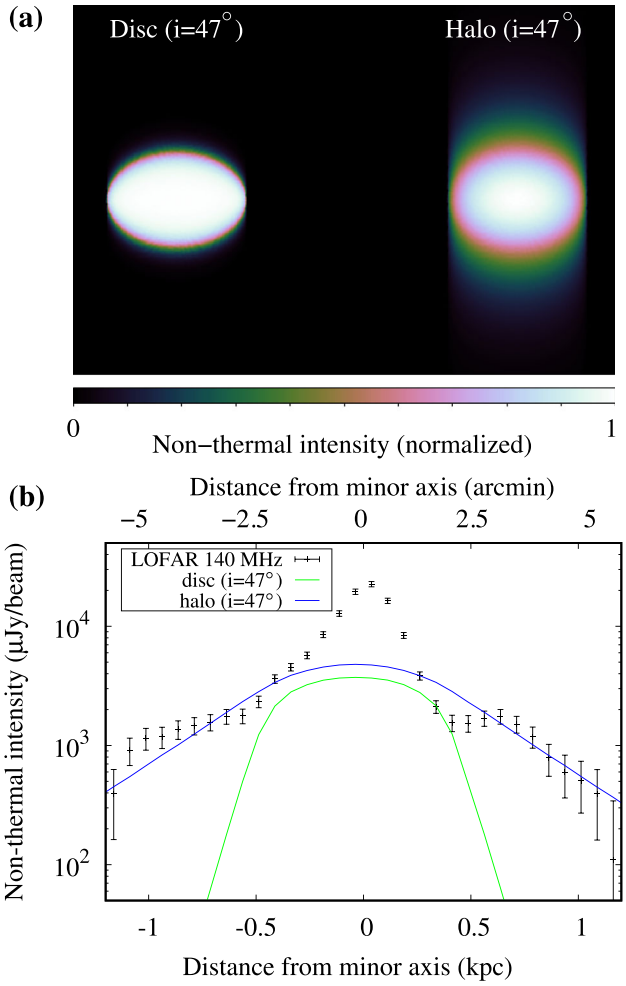

Figure 4. (a) Synthetic non-thermal intensity maps from a 3D toy model of an inclined cylinder of synchrotron emissivity with a vertical intrinsic scale height of either 0.1 kpc (disc model) or 0.5 kpc (halo model). (b) Comparison of the synthetic minor axis profiles of the intensity (arbitrary scaling) with the 140-MHz non-thermal intensity profile (as in Fig. 3). Our toy model does not trace the excess emission at distances <0.5 kpc, which is due to the non-thermal superbubble that is not included in our model.

using the synchrotron emission spectrum of a single CRE. We assume a magnetic field strength of $B_0 = 12\,\mu\mathrm{G}$ in the mid-plane, which comes from the assumption of energy equipartition between the cosmic rays and the magnetic field (Basu et al. 2017). Away from the mid-plane, we explore two basic magnetic field models. (i) We model the magnetic field strength everywhere else to fit the 140-MHz emission, so that as a consequence the 140-MHz intensities are fitted perfectly. A test for the quality of the model is then that the radio spectral index is fitted well. These magnetic field strengths are lower limits since our model assumes that the decrease of the intensities is mostly caused by the decrease of the magnetic field strength rather than CRE energy losses. (ii) We assume a magnetic field strength in approximate agreement with what is expected from energy equipartition. Finally, we assume a ratio of interstellar radiation field to magnetic energy density of $U_{\mathrm{IRF}}/U_B = 0.7$, which is the value found in the non-thermal superbubble (Heesen et al. 2015); this is also the global value if we use the hybrid $\mathrm{H}\alpha + 24\,\mu\mathrm{m}$ calibration (Kennicutt & Evans 2012) to calculate $\mathrm{SFR}_{\mathrm{hyb}} = 0.052\,\mathrm{M}_\odot\,\mathrm{yr}^{-1}$ and convert this to U_{IRF} with a galactocentric radius of $r_{\mathrm{int}} = 0.7$ kpc (Heesen et al. 2016).

Table 1. Best-fitting cosmic ray transport parameters for a CRE injection index of $\gamma_{\rm inj} = 2.0$.

Parameter	North-eastern halo	South-western halo
	Model I: diffusion ($\mu = 0.0$)	
D_0	$2.2^{+0.8}_{-0.6} \times 10^{26}$ cm^2 s^{-1}	$5.0^{+2.3}_{-1.2} \times 10^{26}$ cm^2 s^{-1}
$\chi^2_{\rm red}$	5.5	2.1
dof	10	13
	Model I: diffusion ($\mu = 0.5$)	
D_0	$0.4^{+0.05}_{-0.05} \times 10^{26}$ cm^2 s^{-1}	$0.8^{+0.15}_{-0.16} \times 10^{26}$ cm^2 s^{-1}
$\chi^2_{\rm red}$	3.1	1.5
dof	10	13
	Model II: advection (constant wind speed)	
V_0	20^{+5}_{-3} km s^{-1}	29^{+7}_{-5} km s^{-1}
$\chi^2_{\rm red}$	15	6.3
dof	10	13
	Model III: advection (accelerating wind)	
V_0	14^{+3}_{-3} km s^{-1}	23^{+6}_{-4} km s^{-1}
h_V	0.6 kpc	0.8 kpc
$\chi^2_{\rm red}$	16	10
dof	10	13

Note. μ: parametrization of the energy dependence of the diffusion coefficient with $D = D_0(E/\mathrm{GeV})^\mu$; D_0: diffusion coefficient at 1 GeV; $\chi^2_{\rm red}$: reduced χ^2 of the least-squares fitting with $\chi_{\rm red} = \chi^2/\mathrm{dof}$, where dof is the degrees of freedom; V_0: advection velocity in the galactic mid-plane ($z = 0$); h_V: velocity scale height, so that the advection velocity is $V = V_0 \exp(|z|/h_V)$.

The minor axis profile of the radio spectral index between 140 and 1580 MHz shows the typical 'parabolical' shape for diffusion (Heesen et al. 2016), so that diffusion models fit better than advection models. However, due to the mild inclination we cannot rule out that this is caused by a gradual transition from disc (young CRE) to halo (old CRE) emission. Hence, we have both fitted diffusion and advection models before we will return in Section 5 to discuss both their advantages and issues. The CRE injection index is a free parameter and so is in addition the diffusion coefficient and the advection speed. Since we vary the magnetic field strength to fit the 140-MHz intensities, the number of free parameters is increased further. We found that $\gamma_{\rm inj} = 2.0$ provides the best fit to the data for all models since the non-thermal spectral indices between 140 and 1580 MHz are very flat with $\alpha_{\rm nt} \approx -0.5$. Increasing the injection index to $\gamma_{\rm inj} = 2.1$ leads to poorer fits; as we cannot choose a lower injection index since then no spectral ageing occurs, we use $\gamma_{\rm inj} = 2.0$ in what follows. For diffusion, we parametrized the diffusion coefficient as $D = D_0(E/\mathrm{GeV})^\mu$ and tested models with either $\mu = 0$ (no energy dependence) and with $\mu = 0.5$, applicable for a Kolmogorov-type turbulence (Schlickeiser 2002). In Table 1, we present our best-fitting cosmic ray transport model parameters.

First, we found that for diffusion, energy-dependent diffusion coefficients ($\mu = 0.5$) fit slightly better than ones with no energy dependence ($\mu = 0$). We found that the magnetic field strength has only a small influence on the diffusion coefficients: for energy equipartition in the halo the diffusion coefficients increase by approximately 50 per cent. Second, we fitted advection models with a constant speed. Since advection results in approximately linear vertical spectral index profiles, the fit to the data is of lesser quality than for diffusion. For advection, we did not search for the formally best-fitting model, but for the one that best describes the spectral index decrease in the outskirts of the galaxy (the outermost one or two data points). The reasoning behind this choice is that these data points give us the cleanest estimate of the non-thermal radio spectral index, without the contamination from the emission near the galactic mid-plane. If we were to fit all data points instead, we would overestimate the advection speeds since the contribution to the radio continuum emission from younger CREs near the galactic mid-plane results in too flat non-thermal radio spectral indices. We found that the required advection speeds of ≈20–40 km s^{-1} are well below the escape velocity of 50 km s^{-1}, which we calculated with $V_{\rm esc} = \sqrt{2}V_{\rm rot}$, using a rotation speed of $V_{\rm rot} = 36$ km s^{-1} (Oh et al. 2015). Again, the higher magnetic field strengths from energy equipartition do not change the results much: the advection speeds increase by approximately 50 per cent and are mostly still below the escape velocity.

Finally, we fitted advection models with an accelerating wind, where we assume $V(z) = V_0 \exp(|z|/h_V)$, which adds the velocity scale height, h_V, as an additional free parameter. Because the cosmic ray number density decreases in an accelerating flow due to longitudinal stretching and adiabatic losses, the velocity scale height determines the scale height of the cosmic ray energy density. We chose a velocity scale height of 0.6–0.8 kpc, so that the cosmic rays are approximately in energy equipartition with the magnetic field and dominate over the magnetic field everywhere. We found again that the advection speed near the mid-plane is low, between 11 and 29 km s^{-1}. But due to the acceleration, the escape velocity is exceeded at a height of ≈1 kpc above the mid-plane and at the edge of the observed halo, at $|z| = 1.2$ kpc, the advection speed is ≈100 km s^{-1}. For this model, we did not test the effect of energy equipartition magnetic fields since the field strength is close to energy partition anyway. The best-fitting non-thermal intensity profiles and spectral index profiles are shown in Fig. 3.

5 DISCUSSION

Our best-fitting diffusion coefficients for $\mu = 0.5$ are at least two orders of magnitude smaller than the values of a few 10^{28} cm^2 s^{-1} that are found in the Milky Way and in other external galaxies for CREs with a few GeV, either from a spatial correlation analysis between the radio continuum emission and various star formation tracers (e.g. Berkhuijsen, Beck & Tabatabaei 2013) or from a spectral index analysis as in this work (Heesen et al. 2016; Mulcahy et al. 2016). The larger diffusion coefficients in spiral galaxies could be explained by their more ordered magnetic field structure, where the cosmic rays diffuse along magnetic field lines. This *anisotropic* diffusion can possibly be suppressed in IC 10 due to its turbulent magnetic field structure. The ratio of the ordered to turbulent magnetic field strength, $q = B_{\rm ord}/B_{\rm turb}$, is as small as 0.06 near the two giant H II regions (Chyży et al. 2016). Cosmic ray diffusion is effectively suppressed close to star formation sites (Basu et al. 2017).

Away from the star formation sites in the mid-plane, the field ordering is characterized by $q \approx 0.3$, comparable to what is found in the haloes of spiral galaxies, and anisotropic diffusion becomes a possibility. For a Kolmogorov-type turbulence, the diffusion coefficient parallel to magnetic field lines varies as $D_\parallel \propto q^2 B_{\rm ord}^{-1/3}$ (Schlickeiser 2002). In IC 10, $q = 0.17$ (Chyży et al. 2016), which is half of the value $q = 0.3$ found in late-type spiral galaxies (Fletcher 2010); also $B_{\rm ord} = 2$ μG, which has to be compared with $B_{\rm ord} = 10$–15 μG in the interarm region of spiral galaxies (Beck 2016). Hence, we expect the *anisotropic* diffusion coefficients to be an order of magnitude smaller than in spiral galaxies, or a few 10^{27} cm^2 s^{-1}, which is still at least an order of magnitude too high. As a

consistency check, we can also calculate the diffusion coefficient using an estimate of the CRE diffusion length. The intensity scale height in the north-eastern halo ($z < -0.5$ kpc) is ≈0.35 kpc and in the south-western halo ($z > 0.5$ kpc) it is ≈0.7 kpc. Assuming energy equipartition and a non-thermal radio spectral index of −0.5, the CRE scale height is $h_e = 0.6$–1.2 kpc (cf. equation 11 in Heesen et al. 2009). The CRE lifetime at 140 MHz is $t_{rad} \approx 40$ Myr near the mid-plane ($B = 12$ μG, cf. equation 5 in Heesen et al. 2016). In the halo, the magnetic field strength is lower, so that the lifetime could be larger. However, it is unlikely that the age of the CREs exceeds the duration of the current starburst (the age of the stellar clusters is 4–30 Myr; Hunter 2001). Hence, using $D \approx h_e^2/t_{rad}$, we find values of $D \approx (3\text{–}6) \times 10^{27}$ cm^2 s^{-1}, which again are not in agreement with our values for energy dependence ($\mu = 0.5$).

Alternatively, we consider the possibility that the halo is advection dominated. Using a straightforward estimate for the advection speed of $V \approx h_e/t_{rad}$, we find speeds of $V \approx 15$–30 km s^{-1}, in good agreement for our models with constant advection speeds. In this case, we find that the advection speeds would be well below the escape velocity of ≈50 km s^{-1}. Hence, we have explored also the possibility of an accelerating wind. For this model, we have an additional free parameter in the velocity scale length. We found solutions, where the initial velocity in the mid-plane is similar to the velocity dispersion of both the warm ionized and warm neutral gas (20 ± 5 km s^{-1}; Thurow & Wilcots 2005; Hunter et al. 2012) and increases with height to exceed the escape velocity within 1 kpc distance from the mid-plane. The advantage of an accelerating wind is, besides the sufficient advection speeds, that the cosmic rays are in a self-consistent solution in approximate energy equipartition with the magnetic field. In our model, the cosmic ray energy density is slightly larger than that of the magnetic field, which is expected if the cosmic rays are important in launching the wind. Increasing the cosmic ray energy density in the halo would lead to slower accelerating winds; contrary, a lower cosmic ray energy density would require that the wind accelerates faster.

Fig. 5 shows minor axis profiles of the averaged energy densities of the magnetic field, the warm (≈10^4 K) neutral medium, traced by H I, the warm ionized medium, traced by Hα, and of the cosmic rays. The magnetic energy density is $U_B = B^2/(8\pi)$, and the kinetic energy density of the gas is $U_{kin} = \rho\sigma_v^2/2$, where $\sigma_v = 20 \pm 5$ km s^{-1} is the velocity dispersion. The gas density was measured from either the neutral or ionized hydrogen and includes a correction factor of 1.36 in order to account for the contribution from helium. Since we are interested in a comparison with our 1D cosmic ray transport models, we neglect the error contribution from the variance of the density; thus, the error is solely determined by uncertainty of the velocity dispersion and is $\delta U_{kin} = 2\delta\sigma_v/\sigma_v$, equivalent to 50 per cent. We find that the kinetic energy densities are within a factor of a few in energy equipartition with the magnetic field. This is the expected result since the magnetic field in dwarf galaxies is usually assumed to be amplified by the turbulent gas motions via the 'fluctuating dynamo', which saturates when the energy densities become comparable (Schleicher & Beck 2013). Interestingly in the central part, the magnetic energy density shows a peak that corresponds best to kinetic energy density of the ionized gas, whereas that of the atomic gas is practically constant. The cosmic ray energy density is important everywhere. Such a behaviour has been suggested by theoretical works of cosmic ray-driven galactic winds (e.g. Salem & Bryan 2014), where the cosmic rays can diffuse outwards from star formation sites and thus create an overpressure in the surrounding area. A galactic wind can then be launched in the disc–halo interface, where the cosmic rays dominate the energy density and are able to transfer some of their energy and momentum to the ionized gas via the streaming instability.

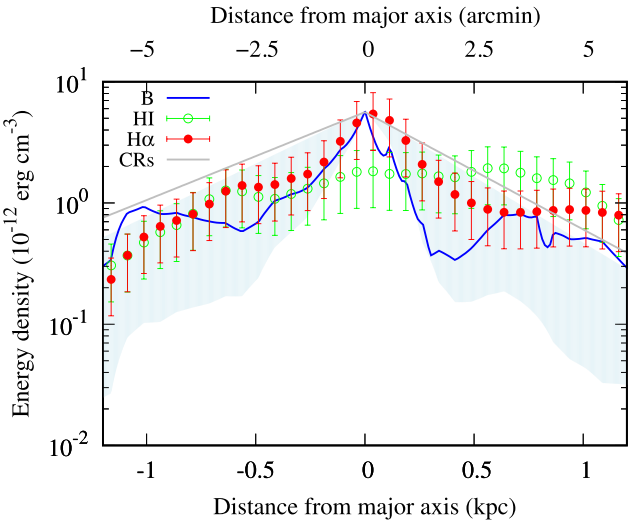

Figure 5. Minor axis profiles with distances from the major axis as seen on the sky. Shown are the energy densities of the magnetic field, warm neutral medium (H I), warm ionized medium (Hα), and cosmic rays (CRs). The blue line shows the magnetic energy density for the accelerating wind model. The blue-shaded area indicates the range of magnetic field strengths for which we tested our models, where the upper limit is for energy equipartition and the lower limit is for almost freely escaping CREs (only radiation losses). Error bars show $\pm 1\sigma$ uncertainties, which are assumed to be 50 per cent stemming solely from the uncertainty of the velocity dispersion (see text for details).

While the diffusion model (Model I) fits our data best, the resulting diffusion coefficients are at least one order of magnitude lower than both estimates for the expected diffusion coefficient. On the other hand, the projected extent of CRE injection sources due to the mild inclination can account for the parabolic shape of the spectral index profile, where the spectral index remains flat out to distances of up to 0.5 kpc away from the major axis; so the abrupt steepening of the spectral index at $|z| > 0.5$ kpc that distinguishes diffusion from advection may be the result of geometry. Hence, we explored the possibility of dominating advection and found that constant wind speeds are only a factor of 2 below the escape velocity – the expected advection speed for a cosmic ray-driven wind (Breitschwerdt, McKenzie & Völk 1993). The remaining discrepancy can be removed by the accelerating wind model (Model III), which also provides us with a self-consistent solution where the magnetic energy density is similar to the kinetic energy densities of the warm neutral and warm ionized medium, while the cosmic rays are dominating by a factor of a few in the halo; this allows the cosmic rays to launch the wind. In summary, we favour Model III that provides us with a physical self-consistent solution even though the fit to the data is poorer than for the diffusion model (Model I).

6 CONCLUSIONS

In this paper, we have presented a low-frequency radio continuum study of the nearby dwarf irregular galaxy IC 10 using new LOFAR data. We have used the facet calibration technique in order to mitigate the effects of the Earth's ionosphere and aperture-array station beams on our observations. Thus, we obtained a deep 140-MHz radio continuum map, which we imaged at 44 arcsec resolution to bring out the weak, diffuse emission. We found that the emission

far away from star formation sites is not very prominent at these low frequencies because the non-thermal radio spectral index is flat, comparable to the injection spectrum. Nevertheless, we found that the radio continuum emission extends further along the minor axis than expected for the inclination angle of IC 10, and intensity profiles along the minor axis show a second, more extended, component away from the disc, which shows the expected behaviour for spectral ageing. We argue that this indicates the existence of a radio halo. The corresponding radio spectral index profile has a shape that can be best explained by diffusion. We then fitted the data with a stationary cosmic ray diffusion model and found diffusion coefficients of $D = (0.4\text{–}0.8) \times 10^{26} (E/\mathrm{GeV})^{0.5}\,\mathrm{cm}^2\,\mathrm{s}^{-1}$. These small diffusion coefficients are likely to be found near star formation sites, where the magnetic field is dominated by the turbulent component and the diffusion happens in an *isotropic* way. In the halo, radio continuum polarimetry observations show a large-scale X-shaped field structure, which would allow the cosmic rays to diffuse *anisotropically* along the magnetic field lines and be advected in a galactic wind (Chyży et al. 2016).

We hence have also explored cosmic ray advection models, assuming that the typical parabolic shape of the radio spectral index profile, which is a telltale sign for diffusion, is the result of a gradual transition from disc to halo emission due to the mild inclination of the galaxy. We found that transport models with constant advection speeds result in best-fitting advection speeds well below the escape velocity. We have thus relaxed the assumption of a constant advection speed and found that our data can also be explained by an accelerating wind. In this model, the wind speed reaches the escape velocity at a height of less than $\approx$1 kpc above the mid-plane. The cosmic ray energy density is everywhere important and the kinetic energy densities of the warm neutral and warm ionized medium are in approximate energy equipartition with the magnetic field. This fulfils the requirement of theoretical models for cosmic ray-driven winds, where the cosmic rays, the magnetic field, and the ionized gas are advectively transported together. Our favourite model is hence that such a wind has developed in IC 10 over the past few tens of Myr – the duration of the current starburst. This is corroborated by the advective time-scales at the edge of the halo ($|z| = 1.2$ kpc) of 27 Myr in the south-western and 37 Myr in the north-eastern halo; they are in good agreement with 30 Myr, the age of the oldest stellar cluster (Hunter 2001).

ACKNOWLEDGEMENTS

We thank the anonymous referee for constructive comments that helped to improve the paper. LOFAR, the Low Frequency Array designed and constructed by ASTRON, has facilities in several countries that are owned by various parties (each with their own funding sources), and that are collectively operated by the International LOFAR Telescope (ILT) foundation under a joint scientific policy. This research was performed in the framework of the DFG Forschergruppe 1254 Magnetisation of Interstellar and Intergalactic Media: The Prospects of Low-Frequency Radio Observations. FST acknowledges financial supports from the Spanish Ministry of Economy and Competitiveness (MINECO) under the grant number AYA2016-76219-P. AF thanks STFC (ST/N00900/1) and the Leverhulme Trust (RPG-2014-427).

REFERENCES

Basu A., Roychowdhury S., Heesen V., Beck R., Brinks E., Westcott J., Hindson L., 2017, MNRAS, 471, 337
Beck R., 2016, A&AR, 24, 4
Bendo G. J., Galliano F., Madden S. C., 2012, MNRAS, 423, 197
Berkhuijsen E. M., Beck R., Tabatabaei F. S., 2013, MNRAS, 435, 1598
Breitschwerdt D., McKenzie J. F., Völk H. J., 1991, A&A, 245, 79
Breitschwerdt D., McKenzie J. F., Völk H. J., 1993, A&A, 269, 54
Burstein D., Heiles C., 1984, ApJS, 54, 33
Chyży K. T., Drzazga R. T., Beck R., Urbanik M., Heesen V., Bomans D. J., 2016, ApJ, 819, 39
Condon J. J., Cotton W. D., Greisen E. W., Yin Q. F., Perley R. A., Taylor G. B., Broderick J. J., 1998, AJ, 115, 1693
Dahlem M., Lisenfeld U., Rossa J., 2006, A&A, 457, 121
Fanaroff B. L., Riley J. M., 1974, MNRAS, 167, 31
Fletcher A., 2010, in Kothes R., Landecker T. L., Willis A. G., eds, ASP Conf. Ser. Vol. 438, The Dynamic Interstellar Medium: A Celebration of the Canadian Galactic Plane Survey. Astron. Soc. Pac., San Francisco, p. 197
Gil de Paz A., Madore B. F., Pevunova O., 2003, ApJS, 147, 29
Heesen V., Beck R., Krause M., Dettmar R.-J., 2009, A&A, 494, 563
Heesen V., Brinks E., Leroy A. K., Heald G., Braun R., Bigiel F., Beck R., 2014, AJ, 147, 103
Heesen V. et al., 2015, MNRAS, 447, L1
Heesen V., Dettmar R.-J., Krause M., Beck R., Stein Y., 2016, MNRAS, 458, 332
Heesen V. et al., 2018a, MNRAS, 474, 5049
Heesen V. et al., 2018b, MNRAS, 476, 158
Hunter D. A., 2001, ApJ, 559, 225
Hunter D. A., Elmegreen B. G., 2004, AJ, 128, 2170
Hunter D. A. et al., 2012, AJ, 144, 134
Kennicutt R. C., Evans N. J., 2012, ARA&A, 50, 531
Kennicutt R. C., Jr, et al., 2009, ApJ, 703, 1672
Lane W. M., Cotton W. D., van Velzen S., Clarke T. E., Kassim N. E., Helmboldt J. F., Lazio T. J. W., Cohen A. S., 2014, MNRAS, 440, 327
McMullin J. P., Waters B., Schiebel D., Young W., Golap K., 2007, in Shaw R. A., Hill F., Bell D. J., eds, ASP Conf. Ser. Vol. 376, Astronomical Data Analysis Software and Systems XVI. Astron. Soc. Pac., San Francisco, p. 127
Massey P., Armandroff T. E., 1995, AJ, 109, 2470
Mulcahy D. D., Fletcher A., Beck R., Mitra D., Scaife A. M. M., 2016, A&A, 592, A123
Niklas S., Beck R., 1997, A&A, 320, 54
Oh S.-H. et al., 2015, AJ, 149, 180
Pakmor R., Pfrommer C., Simpson C. M., Springel V., 2016, ApJ, 824, L30
Rau U., Cornwell T. J., 2011, A&A, 532, A71
Recchi S., Hensler G., 2013, A&A, 551, A41
Rengelink R. B., Tang Y., de Bruyn A. G., Miley G. K., Bremer M. N., Roettgering H. J. A., Bremer M. A. R., 1997, A&AS, 124, 259
Salem M., Bryan G. L., 2014, MNRAS, 437, 3312
Scaife A. M. M., Heald G. H., 2012, MNRAS, 423, L30
Scheers L. H. A., 2011, PhD thesis, Univ. Amsterdam, Amsterdam, the Netherlands
Schleicher D. R. G., Beck R., 2013, A&A, 556, A142
Schlickeiser R., 2002, Cosmic Ray Astrophysics. Springer-Verlag, Berlin
Tabatabaei F. S. et al., 2017, ApJ, 836, 185
Thurow J. C., Wilcots E. M., 2005, AJ, 129, 745
Tremonti C. A. et al., 2004, ApJ, 613, 898
van Haarlem M. P. et al., 2013, A&A, 556, A2
van Weeren R. J. et al., 2016, ApJS, 223, 2
Veilleux S., Cecil G., Bland-Hawthorn J., 2005, ARA&A, 43, 769
Völk H. J., 1989, A&A, 218, 67
Westcott J. et al., 2017, MNRAS, 467, 2113
Williams W. L. et al., 2016, MNRAS, 460, 2385

This paper has been typeset from a TEX/LATEX file prepared by the author.